Magnetic Vortex Nanodiscs Enable Remote Magnetomechanical Neural Stimulation

Danijela Gregurec†,‡,##, Alexander W. Senko†,§,##, Andrey Chuvilin||,#, Pooja D. Reddy§, Ashwin Sankararaman†, Dekel Rosenfeld†,‡, Po-Han Chiang†,‡, Francisco Garcia‡,§, Ian Tafel††, Georgios Varnavides†,§,‡‡, Eugenia Ciocan§§, Polina Anikeeva†,‡,§,|| ||,*

† Research Laboratory of Electronics, Massachusetts Institute of Technology, Cambridge, Massachusetts, 02139, USA

‡ McGovern Institute for Brain Research, Massachusetts Institute of Technology, Cambridge, Massachusetts, 02139, USA

§ Department of Materials Science and Engineering, Massachusetts Institute of Technology, Cambridge, Massachusetts, 02139, USA

|| CIC nanoGUNE, E20018, San Sebastián, Spain

Ikerbasque, Basque Foundation for Science, 48013, Bilbao, Spain

†† Department of Neurosurgery, Brigham and Women's Hospital, Boston, Massachusetts, 02115, USA

‡‡ John A. Paulson School of Engineering and Applied Sciences, Harvard University, Cambridge, Massachusetts, 02138, USA

§§ Department of Engineering and Physical Sciences, Bunker Hill Community College, Boston, Massachusetts, 02129, USA

|| || Department of Brain and Cognitive Sciences, Massachusetts Institute of Technology, Cambridge, Massachusetts, 02139, USA

ABSTRACT. Magnetic nanomaterials in magnetic fields can serve as versatile transducers for remote interrogation of cell functions. In this study, we leveraged the transition from vortex to in-plane magnetization in iron oxide nanodiscs to modulate the activity of mechanosensory cells. When a vortex configuration of spins is present in magnetic nanomaterials, it enables rapid control over their magnetization direction and magnitude. The vortex configuration manifests in near zero net magnetic moment in the absence of a magnetic field, affording greater colloidal stability of magnetic nanomaterials in suspensions. Together, these properties invite the application of magnetic vortex particles as transducers of externally applied minimally invasive magnetic stimuli in biological systems. Using magnetic modeling and electron holography, we predict and experimentally demonstrate magnetic vortex states in an array of colloidally synthesized magnetite nanodiscs 98–226 nm in diameter. The magnetic nanodiscs applied as transducers of torque for remote control of mechanosensory neurons demonstrated the ability to trigger Ca^{2+} influx in weak (≤28 mT), slowly varying (≤5 Hz) magnetic fields. The extent of cellular response was determined by the magnetic nanodisc volume and magnetic field conditions. Magnetomechanical activation of a mechanosensitive cation channel TRPV4 (transient receptor potential vanilloid family member 4) exogenously expressed in the non-mechanosensitive HEK293 cells corroborated that the stimulation is mediated by mechanosensitive ion channels. With their large magnetic torques and colloidal stability, magnetic vortex particles may facilitate basic studies of mechanoreception and its applications to control electroactive cells with remote magnetic stimuli.

KEYWORDS. magnetic nanoparticles, magnetic vortex, electron holography, neuromodulation, mechanosensitive ion channels, cellular signaling, mechanotransduction

Magnetic particles with dimensions near the single-to-multi-domain transition can exhibit a magnetic vortex ground state, where magnetic flux closure is achieved without domain walls (Figure 1). The vortex configuration is more likely to occur in disc-shaped particles made of magnetic materials with high saturation magnetization, which drives the minimization of the magnetostatic energy, and low magnetocrystalline anisotropy and exchange stiffness, which allows for a circular configuration of spins without large energy penalties.[1] Shape anisotropy in magnetic micro- and nanodiscs supports several arrangements of magnetic spins with varied net magnetizations (Figure 1a-c). The negligible net magnetic moment associated with a vortex state in magnetic micro- and nanodiscs minimizes magnetic dipole-dipole interactions between particles and is responsible for their enhanced colloidal stability[2] compared to materials with similar magnetic volumes but uniform spin configurations. This colloidal stability motivated their previous biomedical applications; for example, the transition between vortex and in-plane magnetization states (Figure 1d) in permalloy microdiscs has been leveraged to exert torque on cell membranes in the presence of weak magnetic fields.[3] Microfabricated permalloy microdiscs, however, face challenges regarding their scalable synthesis and long-term chemical stability in physiological environments.[3] Magnetic nanoparticles in combination with high magnetic field gradients have been used to induce magnetic forces to mediate calcium influx in neuronal cells,[4, 5] and high magnetic field gradients have been successfully applied to induce stretching of the cellular membrane and allow for influx of calcium ions on substrates made of magnetic hydrogels.[6] However, these approaches require that neurons are grown in or on specialized substrates, limiting their applicability *in vivo*.

To improve current tools for magnetomechanical modulation of mechanosensory cells, in this study we leveraged magnetic nanodiscs (MNDs) composed of stable magnetite to remotely control mechanosensory cells under weak and slow magnetic fields, motivating the use of MNDs as transducers of signals in biological circuits.

Based on previous methods for fabrication of uniform magnetic nanodiscs[7, 8] with tunable sizes during their hematite phase synthesis[9] and magnetic modeling, we synthesized a broad palette of magnetite MNDs with diameters ranging from 98–226 nm and thicknesses between 24–37 nm. Electron holography was then applied to visualize the alignment of magnetic spins in these MNDs, revealing magnetic vortex states.[10] In weak, slowly varying magnetic fields, MNDs exerted tunable torques on the membranes of mechanosensitive cells, mediating remote control of biological

signaling. Together, these findings indicate that tuning the vortex state in MNDs may be applied to future studies of mechanotransduction and remote torque-dependent switching of nanoscale processes.

RESULTS AND DISCUSSION

Model-driven synthesis and characterization of magnetite nanodiscs.

Tuning the dimensions of magnetite MNDs allowed for the identification of particles that support the magnetic vortex state, while boasting high induced moments in external magnetic fields (MFs). Using The National Institute of Standards and Technology's Object Oriented MicroMagnetic Framework (OOMMF),[11] we constructed a phase diagram showing the highest probability configurations of magnetic spins in magnetite MNDs as a function of their geometric aspect ratio (Figure 1e). We produced an array of MNDs with geometries that were predicted to be capable of supporting the magnetic vortex state (markers in Figure 1e).

The synthesis of anisotropic nanoparticles of the biochemically inert and stable mineral magnetite (Fe_3O_4) is challenging due to its inverse spinel lattice with cubic symmetry, which favors isotropic growth (Figure 2a).[12] To address this challenge we have adapted a high-throughput protocol that relies on a solvothermal synthesis of hematite (α-Fe_2O_3) nanodiscs with a hexagonal lattice, followed by their reduction into magnetite MNDs with conserved dimensions.[13] Briefly, $FeCl_3$, sodium acetate, ethanol and water were heated in an autoclave reactor to generate hematite nanodiscs. After washing in deionized water and drying, the nanodiscs were resuspended in trioctylamine and oleic acid and heated in a hydrogen atmosphere to be converted to magnetite (Figure 2a).

In agreement with Chen et al.,[9] tuning the amount of water in the solution enabled aspect ratio tuning of the hematite nanodiscs. Water molecules allow for hydrogen bonding between the terminating oxygen atoms in the [0001] crystal plane of the hematite and the ligands (ethanol or acetate) present during synthesis, which inhibits the growth in the [0001] direction and results in a decrease in nanodisc diameter.[9] Hematite nanodiscs with mean diameters of 244±37 nm, 181±29 nm, 166±28 nm, 159±26 nm, and 103±24 nm were produced in the presence of 6%, 7%, 8%, 9%, and 10% v/v water in the reaction mixture, respectively (Figure 2b-f). While the hexagonal shape was observed in nanodiscs prepared with 6-9% water (Figure 2b-e), the smallest particles prepared with 10% water displayed more isotropic shapes (Figure 2f). Water content

4

exceeding 10% led to a further decrease in anisotropy, resulting in spheroidal hematite nanoparticles (Supplementary Figure S1).

The reduction of hematite nanodiscs in a hydrogen atmosphere yielded complete conversion of non-magnetic hematite into magnetite while maintaining their geometry (Figure 2g-n, Supplementary Figure S2a). Mean diameters of magnetite nanodiscs were 226±37 nm, 181±17 nm, 170±22 nm, 161±19 nm and 98±12nm for 6%, 7%, 8%, 9%, and 10% v/v water in the starting reaction mixture, respectively (Figure 2l). Scanning electron microscope images of the reduced nanodiscs indicated preservation of their shapes and dimensions (Figure 2g-l), while X-ray diffraction spectra confirmed the transformation from hexagonal hematite into the magnetite inverse spinel phase (Figure 2m, Supplementary Figure S2b-d).[9] This was consistent with the observation that the nanodisc saturation magnetization (M_s) approached that of bulk magnetite (115–120 Am^2/kg_{Fe}) (Figure 2n, Supplementary Figure S2e).[14]

Observation of the magnetic vortex state in magnetite nanodiscs.

Following synthesis and structural characterization, we sought to investigate the ground magnetization state of the magnetite MNDs. Micromagnetic simulations performed using OOMMF indicated that the magnetite MNDs with diameters of 226 nm and 181 nm can assume a vortex state (Figure 3a,b) while the MNDs 98 nm in diameter should exclusively exhibit an in-plane spin configuration (Figure 3c). To test these predictions against experimental data, we employed electron holography, which enables direct interrogation of the magnetization configuration in magnetic nanoparticles.[15] While the vortex state in magnetic anisotropic particles has been extensively studied *via* physical modeling and magnetic force microscopy,[16] the application of electron holography to characterize this state in magnetite nanoparticles has been limited, with no exploration of MNDs with varied dimensions and aspect ratios.[8]

In contrast to OOMMF simulations, electron holography revealed that the magnetic vortex state was not only present in magnetite MNDs with diameters of ~226 nm and ~181 nm but also in smaller ~98 nm MNDs (Figure 3d-f). This illustrated the limitations of the idealized assumptions used in the models. Magnetic field lines contain information on the local arrangement and direction of magnetic spins, where blue and red lines correspond to opposite directions of vortices. Magnetic field lines are not constrained to the magnetic nanodisc due to the eccentricity of the vortex core, which weakly polarizes the particle. As anticipated for the vortex configuration, the particles had

zero net magnetization with no measurable surrounding demagnetization field (Figure 3g-i). The magnetization field in individual particles approached a maximum of 0.6 T locally (Figure 3g,i), corresponding to $M_s = 128$ Am^2/kg_{Fe}, consistent with our measurements (Figure 2n) and bulk values reported for magnetite.[14] In two stacked MNDs we observed vortices with opposite handedness (Figure 3e, red and blue). The stacking and the differences in thickness between the MNDs resulted in overestimation of the magnetic field (up to 2 T) (Figure 3h) and M_s compared to the values measured by ensemble magnetometry (Figure 2n). The magnetization in clustered particles is further determined by the particle arrangement and its direction may partially align with the stack axis (Supplementary Figure S3). Such stacking of MNDs occurs during the sample preparation for electron microscopy and is not anticipated in colloidal solutions, as indicated by dynamic light scattering (DLS) measurements (Supplementary Figure S4).[17]

Application of magnetic nanodiscs as transducers of nanoscale torques on cell membranes.

To render MNDs colloidally stable in physiological fluids and facilitate their attachment to cell membranes, these particles were functionalized with the amphiphilic ligand poly(maleic anhydride-alt-1-octadecene) (PMAO).[18] It has been shown that surfaces with carboxylic groups, such as those resulting from hydrolyzed poly(acrylic acid) or poly(lactic acid), can form bonds with the extracellular protein fibronectin and thereby promote cell attachment.[19, 20] We therefore consider formation of carboxylic groups from hydrolysis of maleic anhydrides to be a plausible mechanism of MND attachment to cells. The presence of the PMAO coating on the MNDs was confirmed by measuring the resulting negative zeta potential of -44±3 mV, and colloidal stability was corroborated *via* DLS (Supplementary Figure S4).

We hypothesized that the transition from a vortex to an in-plane magnetization state under applied magnetic field would allow MNDs decorating the cell membrane to exert torque mimicking biological mechanotransduction (Figure 4a). The torque produced is proportional to the magnetic moment of a MND (which is proportional to the MND volume) and the strength of the applied magnetic field (MF) (Supplementary Information). To illustrate the effects of local MND-mediated torques on cell membranes, we incubated cultures of dorsal root ganglia explants (DRGs) with MNDs (Figure 4b,c, Supplementary Figure S5). DRGs contain sensory neurons expressing a wide range of mechanoreceptors.[21, 22] As mechanotransduction in sensory neurons involves changes in membrane potential and calcium-ion influx (Figure 4a), the effects of magnetically

mediated torques on the cells decorated with MNDs can be monitored *via* the fluorescence change of the Ca^{2+} indicator Fluo-4.

For the same MF conditions, larger MNDs are expected to exert greater torques on the cell membrane, and hence we examined the response of DRG neurons incubated with MNDs 226 nm or 98 nm in diameter. A low MND concentration of 60 µg/ml in Tyrode's solution was sufficient due to electrostatic attachment of MNDs to DRGs. Weak (26 mT), slowly varying (5 Hz) MFs were applied in 10 s epochs separated by 30 s rest periods *via* a custom-built apparatus compatible with simultaneous imaging (Supplementary Figure S6). While the solution temperature remained within 0.5 °C (Figure 4d), a rapid increase in the normalized Fluo-4 fluorescence ($\Delta F/F_0$, where F_0 is the pre-stimulus fluorescence average) was observed in cells decorated with MNDs of either diameter (Figure 4e-h, Supplementary Figure S7a,b, Supplementary Video 1).

As predicted by torque calculations (Supplementary Information), 226 nm MNDs mediated a greater fluorescence increase in the examined cells than the 98 nm MNDs (Figure 4f-h). Negligible responses to MF were found in cells not incubated with MNDs (Figure 4h, Supplementary Figure S7c,d). To further correlate the effects of MF stimulus to the torque-based mechanism, we have examined the responses of MND-decorated hippocampal neurons, which have limited mechanosensitivity.[23] Negligible responses to MF were observed in hippocampal neurons in the presence of 98 nm MNDs (Figure 4h, Supplementary Figure S7e,f). In the presence of 226 nm MNDs, hippocampal neurons responded to MF at a significantly lower rate than the mechanosensitive DRG neurons. This minor, but observable response could likely be attributed in part to the changes in kinetics of ion channels expressed in hippocampal neurons as well as the direct effects on membrane permeability.[5, 23]

To determine the MF magnitude and frequency thresholds for magnetomechanical stimulation, we performed Ca^{2+} imaging of DRGs incubated with MNDs of either 98 nm or 226 nm diameter subjected to MFs of amplitudes from 7–28 mT at either 1 Hz or 5 Hz. We found that the highest frequencies and amplitudes resulted in the highest percentages of responding cells. It is possible that yet higher frequencies and amplitudes would result in even greater responses. The conditions evaluated here were those accessible with our MF apparatus.

To further explore whether the neuronal activation caused by the MND torque is mediated by mechanosensitive ion channels, we specifically inhibited two major mechanoreceptors present in

DRGs. PIEZO2, a recently described mechanosensitive channel, is abundant in DRG neurons and generates robust mechanosensitive cation currents.[21] Another distinct mechanoreceptor in DRGs is the transient receptor potential vanilloid family member 4 (TRPV4).[24] TRPV4 has been shown to be sufficient to impart sensitivity to pN-range forces to non-mechanoreceptive cells.[25]

We first inhibited PIEZO2 by incubating DRG neurons with 1 μM GsMTx4, the venom of the Chilean rose tarantula spider (*Grammostola spatulata*) that specifically blocks PIEZO channels.[26] For selective blocking of TRPV4 we incubated DRGs with 1 μM TRPV4 antagonist, HC-067047.[27] MND-decorated DRGs, incubated with GsMTx4 (Figure 5c, left panel and Supplementary Figure S9a) and HC-067047 (Figure 5c, right panel and Supplementary Figure S9b) displayed similar behavior when MF (5 Hz, 26 mT) was applied. The first 10 s MF pulse produced a fluorescence change similar to trials without drugs, but the following two pulses produced negligible average fluorescence change (Figure 5c, Supplementary Figure S9a,b), indicating that individually inhibiting mechanosensitive channels significantly reduces the efficacy of magnetomechanical stimulation. The delay in the efficacy of the drugs may be due to the need for channel blockers to enter the pore of ion channels before they are inactivated. Similarly, sipatrine, an inhibitor of voltage-gated sodium channels and the mechanosensitive K^+ channels TREK-1 and TRAAK,[28] decreased but did not completely eliminate the response to magnetomechanical stimulation (Supplementary Figure S10a), indicating that the response is mediated by multiple classes of ion channels. In contrast, tetrodotoxin and palmitoleic acid, blockers of sodium channels and gap junctions in neurons and glia, respectively, failed to create any changes in the response to magnetomechanical stimulation, indicating that network effects are not responsible for a significant fraction of the response (Supplementary Figure S10b-d).

Many types of mechanosensitive ion channels have been identified in DRG neurons. Moreover, certain voltage- or ligand-gated channels present in DRGs can also exhibit some mechanosensitivity and contribute to the response to magnetomechanical stimulation.[29, 30] For this reason, we used a non-mechanosensitive cell line, human embryonic kidney (HEK-293) cells, as a test bed for magnetomechanical stimulation (Figure 5d). We also introduced mechanosensitivity to HEK-293 cells using transfection with a *pLenti-CamKIIα::TRPV4-p2A-mCherry* plasmid developed in-house (Supplementary Figure S11a).[31] Naive HEK-293 cells are inactive during application of magnetomechanical stimulation (Figure 5e, left panel), but TRPV4$^+$ HEK-293 cells displayed mechanosensitivity (Figure 5e, middle panel, Supplementary Figure S11b). This

mechanosensitivity was then inhibited with the TRPV4 antagonist HC-067047 (Figure 5e, right panel, Supplementary Figure S11c), confirming that magnetomechanical stimulation with MNDs could be mediated by individual classes of mechanosensitive ion channels.

CONCLUSIONS

While the biocompatibility of isotropic magnetite nanoparticles with dimensions below 100 nm is well documented,[32] the effects of MNDs on cell viability have not yet been explored. Incubating DRG neurons with MNDs for 8 days *in vitro* did not yield significant changes in cell viability (Supplementary Figure S12a). In addition, we investigated whether the MF-mediated torques transduced by MNDs to cell membranes could potentially compromise the membrane integrity. In DRG cultures decorated with 226 nm MNDs, 26 mT, 5 Hz MFs did not yield measurable changes in cell viability (Supplementary Figure S12b-d). This observation indicates that the modest responses to MFs in hippocampal neurons decorated with 226 nm MNDs were likely mediated by the effects of the torque on ion channel gating rather than on membrane permeability.

We hypothesized that switching between the vortex and in-plane magnetization states in anisotropic nanomaterials may permit their use as transducers of torque at the nanoscale. Guided by the predictions of the magnetization state in disc-shaped magnetite particles, we have synthesized an array of MNDs with diameters 98–226 nm and thicknesses 24–37 nm. Electron holography measurements revealed the magnetic vortex ground magnetization state in MNDs with diameters as low as 98 nm. To evaluate the ability of the MNDs to transduce local torques, we applied them to drive the activity of mechanoreceptive sensory neurons in the presence of weak, slowly varying MFs. The extent of the neuronal response was correlated with the MND volume and the MF strength, consistent with a torque-based mechanism. Furthermore, experiments in multiple cell types conducted in the presence of two MND sizes and varying MF parameters indicated that MND-mediated torques drive cellular signaling by activating ion channels involved in mechanotransduction rather than by directly changing the membrane permeability. Our findings indicate that tuning the vortex state in MNDs may be applied to future studies of force transduction at the nanoscale, including the investigation of biological mechanoreception. In the future, it may also be possible to extend our approach to wireless control of neural activity *in vivo*, though delivery of MNDs may present a challenge due to their large dimensions and the need for membrane targeting.

METHODS

Hematite and magnetite nanodisc synthesis. Magnetite nanodiscs were produced based on a two-step process by reducing hematite nanodiscs to magnetite nanodiscs.[8] Hematite nanodiscs were synthesized by mixing 10 mL of absolute ethanol (VWR) and 0.8 g of anhydrous sodium acetate (Sigma-Aldrich) in glass beaker. Size of final magnetite phase was tuned by varying the H_2O amount; 226 nm diameter = 0.6 mL H_2O, 181 nm diameter = 0.7 mL H_2O, 170 nm diameter = 0.8 mL, 161 nm diameter = 0.9 mL H_2O and 98 nm diameter = 1 mL H_2O. The reaction mixture was magnetically stirred until homogenized. Then 0.273 g $FeCl_3 \cdot 6H_2O$ (Fluka) was added and stirred. The homogenized mixture was moved to a Teflon-lined steel vessel, sealed, and heated to 180 °C for 18 h. The red hematite nanodiscs were washed several times with DI H_2O. The clean particles were then dispersed in ethanol and dried in a vacuum desiccator. In all the experiments, ultrapure (UP) water used was produced with a Milli-Q® UV water purification system (Millipore).

Hematite nanodiscs were reduced by adding 20 mL trioctylamine (Sigma-Aldrich) and 1 g oleic acid (Alfa Aesar). The mixture was placed in a three-neck flask connected to a Schlenk line and heated at 20 °C /min to reflux (370 °C) for 25 min in an atmosphere of H_2 (5%) and N_2 (95%). During reduction, the mixture turns from red to a shiny dark grey. Once cooled, the mixture was washed several times with hexane. The clean magnetite particles were then dispersed in chloroform (Sigma-Aldrich) and stored in a glass vial.

Water transfer. MNDs are coated in hydrophobic oleic acid following synthesis so they are functionalized with biocompatible poly(maleic anhydride-alt-1-octadecene) (PMAO) (average M_n 30,000–50,000, Aldrich). First, a 10 mg/mL solution of PMAO in chloroform is prepared. Then this solution is added to dried nanodiscs (1 mg/mL, iron basis). This mixture is then sonicated for one minute and allowed to dry in a vacuum desiccator. When completely dry, TBE buffer (Sigma-Aldrich) was added and the nanodiscs were resuspended *via* sonication at 80 °C for 2 hours. Then the particles were washed with UP H_2O and stored in UP H_2O in a glass vial.

Structural and magnetic characterization. Scanning electron microscopy of hematite and magnetite was performed with a Zeiss Merlin SEM. Transmission electron microscopy and single-particle electron diffraction was performed using an FEI Tecnai G2 Spirit TWIN TEM. Powder X-ray diffraction patterns of as-synthesized hematite and magnetite were collected on a three-

circle diffractometer coupled to a Bruker-AXS Smart Apex charged-coupled-device (CCD) detector with graphite-monochromated Mo Kα radiation (λ = 0.71073 Å) at 300 K. Data were processed with the PANalytical HighScore Plus software. Room-temperature hysteresis curves were generated on a vibrating sample magnetometer (VSM, Digital Measurement Systems Model 880A). An Agilent 5100 Inductively Coupled Plasma-Optical Emission Spectrometer (ICP-OES) was used to quantify the elemental concentration for calculation of saturation magnetization (M_s). For ICP-OES analysis, magnetite nanodiscs were digested in 37% v/v HCl (Sigma-Aldrich) overnight at 60 °C and diluted in 2 wt% HNO_3 (Sigma-Aldrich).

Electron holography imaging and image processing. Electron holography measurements were performed on Titan 60-300 TEM (FEI Co., Netherlands) at 300 kV accelerating voltage in an aberration corrected Lorentz mode. The microscope was equipped with an electron bi-prism at the position of the SA aperture. The bi-prism bias was at about +250V, resulting in interference fringes with a period of about 1.3 nm. In order to extract a magnetic contribution to the phase shift, the samples were *ex situ* flipped and re-measured from the other side. Reconstructed phase images were post-processed in order to account for mirror symmetry, rotation and distortions caused by the corrector. The magnetic contribution to the phase shift was obtained as a difference of the images from two sides. The remnant magnetization was calculated from projected field values assuming average platelet thickness (measured independently).

OOMMF simulations. The National Institute of Standards and Technology's Object Oriented MicroMagnetic Framework (OOMMF)[11] was used to simulate MNDs. A mask was used to define the hexagonal shape of a MND, and the MND was subdivided into 125 nm^3 elements, each with a random initial magnetization direction. OOMMF then implements an energy minimization algorithm to find the lowest-energy configuration of element magnetizations (each element is treated as uniformly magnetized). The expected equilibrium domain states were in-plane, out-of-plane, and vortex, though sometimes intermediate phases were observed. An automated phase classification scheme was developed, in which the net in-plane and out-of-plane magnetization character of each simulated MND was calculated and converted to an RGB color value. This color value was plotted for MNDs with a range of dimensions and the result was a phase diagram indicating, for a given MND size, what the default magnetic domain state is. Ten simulations for each geometry of MND were performed and the results averaged. A color between those corresponding to the canonical phases generally indicates that some initial conditions led to one

canonical phase and others led to a different canonical phase, or in some cases an intermediate phase.

Magnetic field system. A 10 lb spool of 16 AWG magnet wire was purchased from MWS Wire Industries. The centre of this spool was removed to create a large-bore solenoid. A commercial magnetic field (MF) probe (Lake Shore Cryotronics) was used to measure the field/current relationship for the solenoid, and during experiments the current was measured *via* the voltage across a 0.5 ohm shunt resistor connected in series with the solenoid. The measured current and the established field/current relationship was used to infer the MF amplitude. The solenoid/resistor circuit was driven by a Crown DC-300 power amplifier with a 3 V_{P-P}, 5 Hz input signal from a function generator.

***In vitro* studies.** All the experimental procedures involving primary cultures were approved by the MIT Committee on Animal Care.

Dorsal root ganglion (DRG) culture. 12 mm round glass cover slips were coated with 70 uL Matrigel® solution (Corning®) (Matrigel® diluted 30x in Neurobasal™ medium with serum-free B27™ Supplement (both Gibco, ThermoFisher)) overnight prior to DRG seeding. Whole DRGs from P0 Sprague-Dawley rat pups were seeded individually on cover slips in a 24-well plate with 1 mL Neurobasal™ medium with serum-free B27™ supplement per well and kept in incubator at 37 ºC and 5% CO_2.

Hippocampal neuron culture. Hippocampi were extracted from pups of Sprague-Dawley rats at post-natal day 0 in cold dissection solution (160 mM NaCl, 5 mM KCl, 1 mM $MgSO_4$, 4 mM $CaCl_2$, 5 mM HEPES, 5.5 mM Glucose, adjusted to pH 7.4 by NaOH). To dissociate hippocampal neurons, extracted hippocampi were transferred into pre-warmed digestion solution (1 mM $CaCl_2$, 1.5 mM NaOH, 0.5 mM EDTA, 1 mM L-cysteine, and 10 units/ml papain (Worthington Biochemical) in dissection solution) and incubated at 37 °C for 25 min. Digestion was stopped by incubating in inhibition solutions (0.25% trypsin inhibitor and 0.25% bovine albumin, 0.4 % D-glucose, and 5% fetal bovine serum (FBS; Gibco, ThermoFisher) in Minimum Essential Medium (MEM) w/Earl's Balanced Salt w/o L-glutamine) at 37 °C for 2 min. After removing inhibition solutions and triturating dissociated cells with serum medium (0.4% D-glucose and 5% FBS in MEM w/Earl's Balanced Salt w/o L-glutamine), cells were seeded in 24-well plates with ~80,000 cells/well. Hippocampal cells were maintained in culture medium (Neurobasal™-A medium with

serum-free B27^{TM} Supplement and GlutaMAX™; Gibco^{TM}). Glial cells were inhibited by adding mitotic inhibitor (4 µM 5-fluoro-2'-deoxyuridine and 10 µM uridine in culture medium) into hippocampal culture at 3 days *in vitro* (DIV). All the imaging and stimulation are performed at 7–14 DIV.

HEK-293 cell culture and TRPV4 transfection. The HEK-293FT cell line was a gift from the lab of Feng Zhang (MIT). Cells were cultured in Dulbecco's Modified Eagle Medium (DMEM) w/ GlutaMAX™ supplemented with 10% FBS. For imaging, HEK cells were cultured on 12 mm round coverslips which were coated with Matrigel® Matrix solution (Corning; Matrigel diluted 30x in DMEM with 10% FBS) overnight prior to cell seeding in 24-well plate. When cells reach 70% confluency, transfection was performed by adding a mixture of 1 µl Lipofectamine® 2000 and 0.5 µg of sDNA plasmid (pLenti-CamKIIα::TRPV4-p2A-mCherry) in 50 µl of Opti-MEM. Cells were used for imaging after 24–48 hours of transfection.

Magnetomechanical stimulation. Magnetomechanical stimulation was evaluated by performing Ca^{2+} imaging on DRG explant culture, as well as control cultures of hippocampal neurons and HEK cells decorated with MNDs and applying low frequency MF *in situ*. 1 mM Fluo-4 AM (Invitrogen) in DMSO (Sigma-Aldrich) was diluted 1000x in Neurobasal^{TM} medium with serum-free B27^{TM} supplement for DRG and hippocampal neurons. For HEK-293 cell culture, DMEM with 10% FBS was used. Cells were incubated in this solution for 45 minutes and then transferred to Tyrode's solution. 30 µL of magnetite nanodiscs at a concentration of 2 mg/mL were added to each well and the 24-well plate was gently shaken to disperse magnetite nanodiscs. After 15 minutes of incubation, DRGs on coverslips were extracted from the 24-well plate, excess magnetite nanodiscs were washed off, and the coverslips with DRGs were placed into a custom imaging chamber surrounded by a solenoid mounted onto an inverted microscope. Following a 5 min equilibration period, we have performed the Ca^{2+} imaging experiments. During the experiment, slowly varying MFs were applied in 10 s pulses at intervals of 30 s.

Pharmacology experiments. The magnetomechanical stimulation and Ca^{2+} imaging experiment described above was modified by adding drugs. The PIEZO-specific inhibitor GsMTx4 (Smartox) was added to Tyrode's solution at a concentration of 1 µM. 1 µM of the TRPV4 antagonist HC-067047 (MilliporeSigma) was added to the DRGs and HEK-293 cells transfected with TRPV4 and Ca^{2+} imaging began after 25 m of incubation. During the experiments, slowly varying MF (5 Hz,

26 mT) was applied in 10 s pulses at intervals of 30 s.

Calcium imaging analysis. Videos of calcium activity were collected on an inverted Olympus IX73 microscope in the .vsi format using the Olympus cellSens software. The frame rate was 4 Hz. The .vsi files were processed in ImageJ with the Bioformats package. The "Threshold", "Watershed", and "Analyze Particles" functions were used to delineate, separate, and circle cells automatically, respectively. The average grayscale value in the regions of interest (ROIs) generated this way was exported in a .csv file and processed with MATLAB (MathWorks). A custom MATLAB script was used to convert the average grayscale value of each ROI over time into $\Delta F/F_0$ traces using the algorithm described in Box 1 of Jia *et al.*,[33] with $\tau_0 = 0.75$ s, $\tau_1 = 2.5$ s, and $\tau_2 = 7.5$ s, but with the modification that a central moving average and F_0 calculation was used instead of a simple moving average. A second MATLAB script was used for choosing at random a subset of 50 cells from each experiment and classifying them as responsive or non-responsive based on whether their $\Delta F/F_0$ trace ever exceeds 10 times the standard deviation of the signal during the period before MF is ever applied. Heatmaps displaying $\Delta F/F_0$ *vs*. time were generated in Mathematica (Wolfram).

Cell viability and biocompatibility assay. The Invitrogen LIVE/DEAD® Viability/Cytotoxicity kit was used to assess whether magnetomechanical stimulation or exposure to MNDs caused cytotoxicity. The kit uses calcein AM (green) to mark live cells and ethidium homodimer-1 (red) to mark dead cells. The stock solutions were both diluted in a single mixture containing 400 nM of both dyes. Immediately before and 30 minutes after stimulation, DRGs were imaged with an inverted microscope, and images were processed with a MATLAB script: each region was imaged with both red and green filters; the relative abundance of green cells and red cells (by area) was tabulated for each region for each condition, with 100% live cells corresponding to all cell area being green and none being red.

The biocompatibility of magnetite nanodiscs was examined using the alamarBlue metabolic assay (Thermo Scientific). DRGs were incubated on day 0 with alamarBlue solution (1:10 in cell medium) for 4 hours followed by fluorescence intensity reading using a plate reader with 545 nm excitation and 590 nm emission detection. Magnetite nanodiscs at concentration of 0.8 mg/ml were then added to each well with DRGs and incubated at 37 °C while monitoring the DRG growth. The alamarBlue assay was repeated as described after 24 hours, 4 days and 8 days of

culture. Cell viability and proliferation rate compared to the day 0 baseline was evaluated.

Immunohistochemistry. DRGs were seeded on coverslips and, following a 2-week growth period, fixed for 20 min in 4% paraformaldehyde. After three washes with PBS, cells were permeabilized with 0.3% (vol/vol) Triton X-100 for 10 minutes and blocked with 2.5% donkey serum in PBS overnight at 4 °C. Cells were incubated for 2 hours at room temperature with primary antibody (rabbit anti-Neurofilament 1:500 (Sigma N4142) and mouse anti-S100 1:500 (Sigma S2532)) with 2.5% donkey serum in PBS. After 3 washes of the cells with PBS, incubation with matching secondary antibody in PBS was performed (donkey anti-rabbit Alexa Fluor 488 (Invitrogen A21206) and donkey anti-mouse Alexa Fluor 568 (Invitrogen A10037), respectively, 1:1000) for 2 hours and with DAPI (4'6-diamidino-2-phenylindole)(1:50,000) for another 15 minutes, and washed three times with PBS. Coverslips were mounted onto glass microscope slides using mounting solution (Fluoromount-G®, SouthernBiotech).

Statistical analysis. Statistical differences were determined using a two-way ANOVA and a post-hoc Tukey's honest significant difference test.

Crystal structure drawing. Crystal structures of hematite and magnetite were prepared using the VESTA structure analysis software.[34]

Data availability

The data that support the findings of this study are available within the manuscript and supplementary information.

ASSOCIATED CONTENT

Supporting Information Available

The Supporting Information is available free of charge at:

Supplemental file on: Calculations of magnetic forces, Nanodisc characterization, Description of magnetic coil setup, Biocompatibility experiments, Control *in vitro* experiments

Video of magnetomechanical stimulation during a calcium imaging experiment

CIF structure files

Custom analysis MATLAB scripts for analysis of grayscale values from Ca^{2+} imaging videos.

Preprint available

Corresponding author

Email: anikeeva@mit.edu

Author contributions

The manuscript was written through contributions of all authors. All authors have given approval to the final version of the manuscript. ## These authors contributed equally.

Competing financial interest statement

P.A., A.W.S., D.G., and P.D.R. are co-authors on a patent application based on this work.
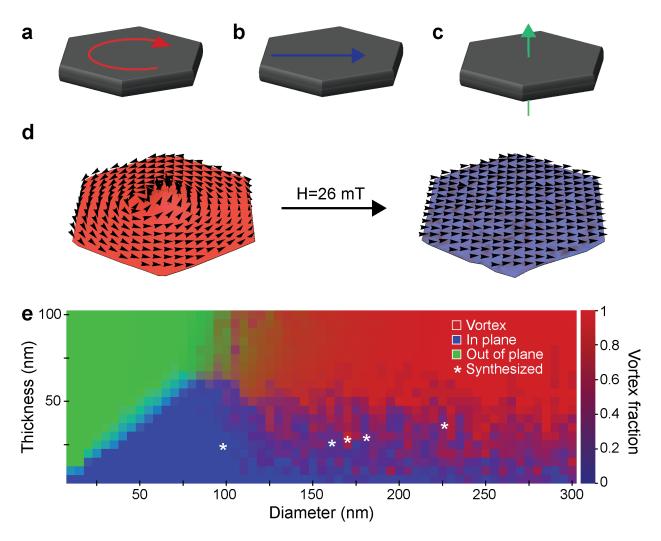
Acknowledgments

References

1. Parreiras, S. O.; Martins, M. D. Effect of Planar Anisotropy in Vortex Configuration of Micro-Scale Disks. *Phys. Procedia* **2015,** *75*, 1142-1149.
2. Lisjak, D.; Mertelj, A. Anisotropic Magnetic Nanoparticles: A Review of Their Properties, Syntheses and Potential Applications. *Prog. Mater. Sci.* **2018,** *95*, 286-328.

3. Kim, D.-H.; Rozhkova, E. A.; Ulasov, I. V.; Bader, S. D.; Rajh, T.; Lesniak, M. S.; Novosad, V. Biofunctionalized Magnetic-Vortex Microdiscs for Targeted Cancer-Cell Destruction. *Nat. Mater.* **2009,** *9*, 165-171.

4. Tay, A.; Di Carlo, D. Magnetic Nanoparticle-Based Mechanical Stimulation for Restoration of Mechano-Sensitive Ion Channel Equilibrium in Neural Networks. *Nano Lett.* **2017,** *17*, 886-892.

5. Tay, A.; Kunze, A.; Murray, C.; Di Carlo, D. Induction of Calcium Influx in Cortical Neural Networks by Nanomagnetic Forces. *ACS Nano* **2016,** *10*, 2331-2341.

6. Tay, A.; Sohrabi, A.; Poole, K.; Seidlits, S.; Di Carlo, D. A 3D Magnetic Hyaluronic Acid Hydrogel for Magnetomechanical Neuromodulation of Primary Dorsal Root Ganglion Neurons. *Adv. Mater.* **2018,** *30*, 1800927.

7. Yang, Y.; Li, M.; Wu, Y.; Zong, B.; Ding, J. Size-Dependent Microwave Absorption Properties of Fe3O4 Nanodiscs. *RSC Adv.* **2016,** *6*, 25444-25448.

8. Yong, Y.; Xiaoli, L.; Yunbo, L.; Seng, H. T.; Xianhui, X.; Weixing, X.; Taishi, Z.; Jie, F.; Wen, X.; Jun, D. Orientation Mediated Enhancement on Magnetic Hyperthermia of Fe3O4 Nanodisc. *Adv. Funct. Mater.* **2015,** *25*, 812-820.

9. Chen, L.; Yang, X.; Chen, J.; Liu, J.; Wu, H.; Zhan, H.; Liang, C.; Wu, M. Continuous Shape- and Spectroscopy-Tuning of Hematite Nanocrystals. *Inorg. Chem.* **2010,** *49*, 8411-8420.

10. Ammar, M.; LoBue, M.; Snoeck, E.; Hÿtch, M.; Champion, Y.; Barrué, R.; Mazaleyrat, F. A Quantitative Analysis of Magnetic Vortices in Permalloy Nanoparticles Characterized by Electron Holography. *J. Magn. Magn. Mater.* **2008,** *320*, e716-e719.

11. Donahue, M. J., *Oommf User's Guide [Microform] / M.J. Donahue, D.G. Porter*. U.S. Dept. of Commerce, Technology Administration, National Institute of Standards and Technology: Gaithersburg, MD, 1999.

12. Mann, S.; Sparks, N. H. C.; Blakemore, R. P. Structure, Morphology and Crystal Growth of Anisotropic Magnetite Crystals in Magnetotactic Bacteria. *Proc. R. Soc. London, Ser. B* **1987,** *231*, 477-487.

13. Zhu, M.; Wang, Y.; Meng, D.; Qin, X.; Diao, G. Hydrothermal Synthesis of Hematite Nanoparticles and Their Electrochemical Properties. *J. Phys. Chem. C* **2012,** *116*, 16276-16285.

14. Kemp, S. J.; Ferguson, R. M.; Khandhar, A. P.; Krishnan, K. M. Monodisperse Magnetite Nanoparticles with Nearly Ideal Saturation Magnetization. *RSC Adv.* **2016,** *6*, 77452-77464.

15. Dunin - Borkowski, R. E.; Kasama, T.; Wei, A.; Tripp, S. L.; Hÿtch , M. J.; Snoeck, E.; Harrison, R. J.; Putnis, A. Off-Axis Electron Holography of Magnetic Nanowires and Chains, Rings, and Planar Arrays of Magnetic Nanoparticles. *Microsc. Res. Tech.* **2004,** *64*, 390-402.

16. Yang, Y.; Liu, X.-L.; Yi, J.-b.; Yang, Y.; Fan, H.-M.; Ding, J. Stable Vortex Magnetite Nanorings Colloid: Micromagnetic Simulation and Experimental Demonstration. *J. Appl. Phys.* **2012,** *111*, 044303.

17. Fissan, H.; Ristig, S.; Kaminski, H.; Asbach, C.; Epple, M. Comparison of Different Characterization Methods for Nanoparticle Dispersions Before and After Aerosolization. *Anal. Methods* **2014,** *6*, 7324-7334.

18. Pichaandi, J.; Abel, K. A.; Johnson, N. J. J.; van Veggel, F. C. J. M. Long-Term Colloidal Stability and Photoluminescence Retention of Lead-Based Quantum Dots in Saline Buffers and Biological Media through Surface Modification. *Chem. Mater.* **2013,** *25*, 2035-2044.

19. Chiang, E. N.; Dong, R.; Ober, C. K.; Baird, B. A. Cellular Responses to Patterned Poly(Acrylic Acid) Brushes. *Langmuir* **2011,** *27*, 7016-7023.

20. Nagai, M.; Hayakawa, T.; Makimura, M.; Yoshinari, M. Fibronectin Immobilization Using Water-Soluble Carbodiimide on Poly-L-Lactic Acid for Enhancing Initial Fibroblast Attachment. *J. Biomater. Appl.* **2006,** *21*, 33-47.

21. Coste, B.; Mathur, J.; Schmidt, M.; Earley, T. J.; Ranade, S.; Petrus, M. J.; Dubin, A. E.; Patapoutian, A. Piezo1 and Piezo2 Are Essential Components of Distinct Mechanically Activated Cation Channels. *Science* **2010,** *330*, 55-60.

22. Ranade, S. S.; Syeda, R.; Patapoutian, A. Mechanically Activated Ion Channels. *Neuron* **2015,** *87*, 1162-1179.

23. Paoletti, P.; Ascher, P. Mechanosensitivity of NMDA Receptors in Cultured Mouse Central Neurons. *Neuron* **1994,** *13*, 645-655.

24. Cao, D.-S.; Yu, S.-Q.; Premkumar, L. S. Modulation of Transient Receptor Potential Vanilloid 4-Mediated Membrane Currents and Synaptic Transmission by Protein Kinase C. *Mol. Pain* **2009,** *5*, 5-5.

25. Matthews, B. D.; Thodeti, C. K.; Tytell, J. D.; Mammoto, A.; Overby, D. R.; Ingber, D. E. Ultra-Rapid Activation of TRPV4 Ion Channels by Mechanical Forces Applied to Cell Surface Beta1 Integrins. *Integr. Biol.* **2010,** *2*, 435-442.

26. Bae, C.; Sachs, F.; Gottlieb, P. A. The Mechanosensitive Ion Channel Piezo1 Is Inhibited by the Peptide GsMTx4. *Biochemistry* **2011,** *50*, 6295-6300.

27. Garcia-Elias, A.; Mrkonjic, S.; Pardo-Pastor, C.; Inada, H.; Hellmich, U. A.; Rubio-Moscardo, F.; Plata, C.; Gaudet, R.; Vicente, R.; Valverde, M. A. Phosphatidylinositol-4,5-Biphosphate-Dependent Rearrangement of TRPV4 Cytosolic Tails Enables Channel Activation by Physiological Stimuli. *Proc. Natl. Acad. Sci. U. S. A.* **2013,** *11*, 9553-9558.

28. Meadows, H. J.; Chapman, C. G.; Duckworth, D. M.; Kelsell, R. E.; Murdock, P. R.; Nasir, S.; Rennie, G.; Randall, A. D. The Neuroprotective Agent Sipatrigine (Bw619c89) Potently Inhibits the Human Tandem Pore-Domain K(+) Channels TREK-1 and TRAAK. *Brain Res.* **2001,** *892*, 94-101.

29. Gu, C. X.; Juranka, P. F.; Morris, C. E. Stretch-Activation and Stretch-Inactivation of Shaker-Ir, a Voltage-Gated K+ Channel. *Biophys. J.* **2001,** *80*, 2678-2693.

30. Mienville, J.; Barker, J. L.; Lange, G. D. Mechanosensitive Properties of Bk Channels from Embryonic Rat Neuroepithelium. *J. Membr. Biol.* **1996,** *153*, 211-216.

31. Avci-Adali, M.; Behring, A.; Keller, T.; Krajewski, S.; Schlensak, C.; Wendel, H. P. Optimized Conditions for Successful Transfection of Human Endothelial Cells with *In Vitro* Synthesized and Modified mRNA for Induction of Protein Expression. *J Biol Eng* **2014,** *8*, 8-8.

32. Chen, R.; Romero, G.; Christiansen, M. G.; Mohr, A.; Anikeeva, P. Wireless Magnetothermal Deep Brain Stimulation. *Science* **2015,** *347*, 1477-1480.

33. Jia, H.; Rochefort, N. L.; Chen, X.; Konnerth, A. *In Vivo* Two-Photon Imaging of Sensory-Evoked Dendritic Calcium Signals in Cortical Neurons. *Nat. Protoc.* **2010,** *6*, 28-35.

34. Momma, K.; Izumi, F., Vesta 3 for Three-Dimensional Visualization of Crystal, Volumetric and Morphology Data. *J. Appl. Crystallogr.* **2011,** *44*, 1272-1276.

Figure 1: The magnetic vortex phase in magnetite nanodiscs.

a-c, Schematic representation of the three possible configurations of magnetic spins in magnetite nanodiscs (MNDs); **a**, vortex, **b**, in-plane and **c**, out-of-plane. **d**, MND that supports the magnetic vortex state (left) in the absence of applied magnetic field can transition to being magnetized in-plane (right) upon the application of a weak magnetic field. **e**, MNDs with a range of thicknesses and diameters were each simulated 10 times using OOMMF, and their average final configuration was plotted to create a magnetic domain state phase diagram. For points with an intermediate color, either the equilibrium phase is a hybrid of the three canonical phases or two distinct equilibrium phases can result from different initial conditions in the simulation. White star markers on the phase diagram represent five MND compositions synthesized and used for experiments in this study.
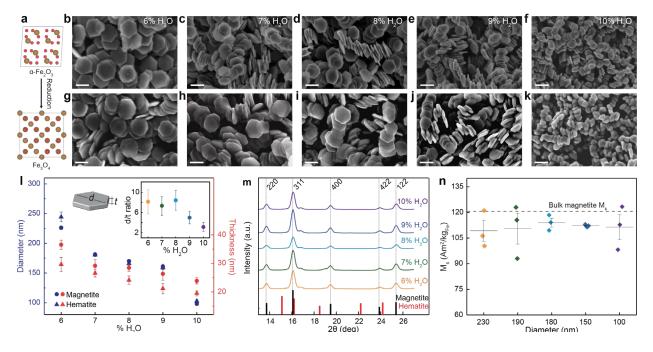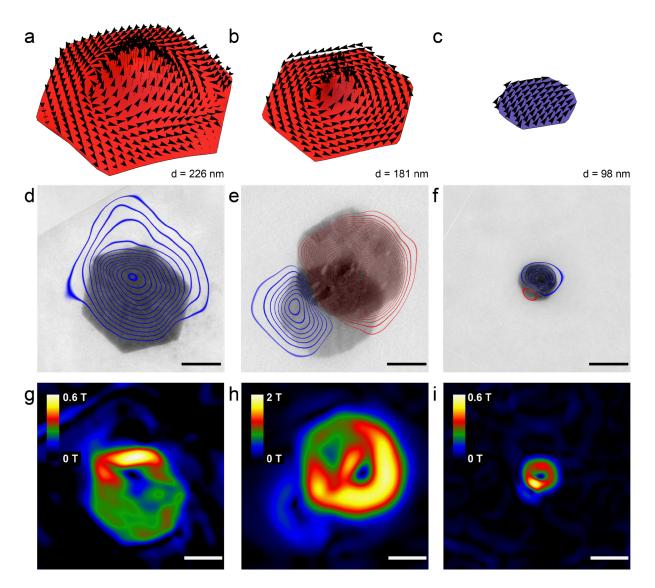
Figure 2: Synthesis and characterization of magnetite nanodiscs.

a, Crystal units of non-magnetic hematite phase converted to magnetic magnetite after reduction. Nanodiscs synthesized in two-step solvothermal reaction with 6% H_2O (**b,g**), 7% H_2O (**c,h**), 8% H_2O (**d,i**), 9% H_2O (**e,j**) and 10% H_2O. (**f,k**). **b-f** are hematite structures (α-Fe_2O_3) resulting from the first step of the synthesis. **g-k** are magnetite structures (Fe_3O_4) derived from the reduction of hematite discs. Scale bars = 200 nm. **l**, Diameter (blue, left axis) and thickness (red, right axis) of nanodiscs before and after reduction as a function of the percentage of H_2O in the synthesis (inset: calculated d/t ratio). **m**, XRD spectra for MNDs after reduction (hematite reference in red, magnetite reference in black). **n**, Saturation magnetization for MNDs and reference to saturation magnetization of bulk magnetite shown (dashed line).[14]

Figure 3: Simulations and experimental study of vortex state in magnetite nanodiscs.

a-c, Magnetization configuration emerging from micromagnetic simulation of MNDs 226 nm, 181 nm, or 98 nm in diameter, respectively. **d-i**, Electron holography on MNDs: magnetic field lines overlapping the magnetic nanodiscs 226 nm, 181 nm or 98 nm in diameter, respectively. Blue and red lines denote vortices of opposite directions. **g-i**, Corresponding magnetization of upper images. Scale bars = 100 nm.
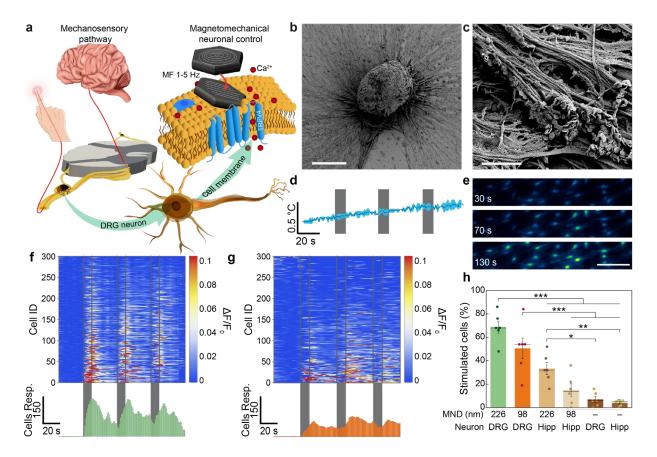
Figure 4: Magnetomechanical stimulation of MND-decorated DRG neurons allows for remote activation of Ca²⁺ influx.

a, DRGs relay sensory information, including mechanosensory information, to the spinal cord. DRG explants incubated with MNDs can be stimulated when slowly varying MFs cause MNDs to transition from vortex to in-plane magnetization, producing forces on mechanosensitive ion channels and resulting in Ca^{2+} influx. **b**, Scanning electron microscope image of DRG explant culture incubated with MNDs. Scale bar = 200 µm. **c**, Detail of a region of the DRG. Individual MNDs are visible on the surface. Scale bar = 2 µm. **d**, Bath temperature monitored during a magnetomechanical stimulation experiment. Shaded area represents standard error. **e**, False color stills from a representative video of DRG explant culture loaded with the Ca^{2+} indicator Fluo-4 and subject to magnetomechanical stimulation. Scale bar = 50 µm. 5 Hz, 26 mT MF stimulation of DRGs decorated with MNDs 226 nm (**f**) and 98 nm (**g**) in diameter. Heat maps (top) represent the fluorescence change of individual cells during the experiment. On the same time axis are plotted the total number of responding cells at any time (bottom). **h**, Comparison of the efficacy of magnetomechanical stimulation for 226 nm and 98 nm diameter MNDs on DRGs. A two-way

ANOVA was conducted on the influence of culture type (DRG or hippocampal neurons) and MND type (226 nm, 98 nm, and none) on the percentage of stimulated cells in calcium imaging. The main effect for MND type yielded an F-test statistic of $F_{2,30} = 38$, $p = 5.6 \times 10^{-9}$ (where in $F_{x,y} = z$, x is number of degrees of freedom (df) for the factor of interest (*e.g.*, MND type), y is df for the error, and z is the F-test statistic (*i.e.,* the ratio of the mean square error (MSE) between groups to the MSE within groups), and p is the probability, given a chance model in which the means of each group are the same, of observing this F-test statistic). The main effects for culture type and the interaction were also significant ($F_{1,30} = 33$, $p = 2.8 \times 10^{-6}$ and $F_{2,30} = 6.4$, $p = 4.9 \times 10^{-3}$, respectively). In all experiments, MF is applied in 3 epochs of 10 s as shown in shaded grey regions. The cell number per condition is 300, and the number of experiments per condition is n = 6. Post-hoc testing was performed for pairwise comparison of means using Tukey's honest significant difference method; all *p*-values are listed in Supplementary Table 1. * $p \leq 0.05$, ** $p \leq 0.01$, *** $p \leq 0.001$.
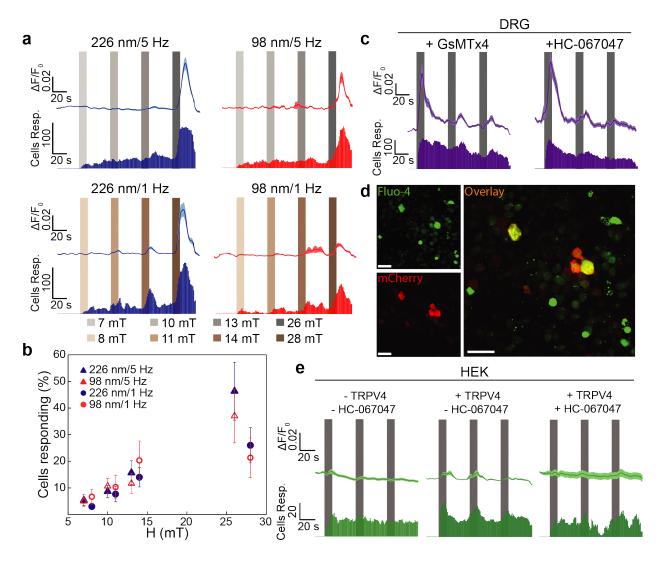
Figure 5: Tuning parameters for magnetomechanical stimulation in DRG neurons and demonstration of magnetomechanical stimulation in HEK-293 cells transfected with TRPV4. **a**, Fluorescence traces resulting from stimulation of DRG neurons incubated with 226 nm diameter MNDs (left) and 98 nm diameter MNDs with MF frequencies of 5 Hz (top) and 1 Hz (bottom). MF amplitude is sequentially increased from 7 mT to 28 mT (marked by the shaded regions). MF is applied in 4 pulses of 10 s with 30 s wait times between pulses. **b**, Summary of cell response rate for conditions permuted in (**a**). Error bars represent standard error of the mean. **c**, DRGs incubated with 1 μM piezo inhibitor GsMTx4 (left) and with TRPV4 antagonist HC-067047 (right) both show a decrease in activity after the first stimulation sequence. **d**, Confocal images of HEK-293 cells loaded with the calcium indicator Fluo-4 and transfected with the mechanosensitive TRPV4 channel labeled with mCherry. Scale bars = 100 μm. **e**, The response of unmodified HEK-293 cells decorated with MNDs to MF application (left), the response of HEK-293 cells expressing

TRPV4 decorated with MNDs to MF application (middle), and the blocked response of HEK-293 cells decorated with MNDs, expressing TRPV4, and incubated 1 µM TRPV4 antagonist, HC-067047 (right). In experiments shown in (**c**) and (**e**), a 5 Hz, 26 mT MF is applied in 3 sequences of 10 s as shown in the shaded grey regions. The number of cells per condition is 300. Standard error is represented by shaded area in fluorescence traces.